

# Spatial Discontinuity-Weighted Sparse Unmixing of Hyperspectral Images

Shaoquan Zhang<sup>1</sup>, *Student Member, IEEE*, Jun Li, *Senior Member, IEEE*, Zebin Wu<sup>2</sup>, *Member, IEEE*,  
and Antonio Plaza<sup>3</sup>, *Fellow, IEEE*

**Abstract**—Spectral unmixing is an important technique for remotely sensed hyperspectral image interpretation, of which the goal is to decompose the image into a set of pure spectral components (endmembers) and their abundance fractions in each pixel of the scene. Sparse-representation-based approaches have been widely studied for remotely sensed hyperspectral unmixing. A recent trend is to incorporate the spatial information to improve the spectral unmixing results. Those methods generally assume that the abundances of the pixels are piecewise smooth and fall into a homogeneous region occupied by the same endmembers and their corresponding fractional abundances. However, in real scenarios, abundances may vary abruptly from pixel to pixel. Therefore, the former assumption in most spatial models does not hold. To address this limitation, we propose a new strategy to preserve the spatial details in the abundance maps via a spatial discontinuity weight. Our experimental results, conducted with both simulated and real hyperspectral data sets, illustrate the good potential of our discontinuity-preserving strategy for sparse unmixing, which can greatly improve the abundance estimation results.

**Index Terms**—Discontinuity-preserving spatial weight, hyperspectral imaging, sparse unmixing, spatial information.

## I. INTRODUCTION

**H**YPERSPECTRAL remote sensing sensors collect spectral information from the earth's surface using hundreds of narrow and contiguous wavelength bands [1]. It has been widely applied in various fields, such as target detection [2]–[4], material mapping [5], and material identification [6]. However, due to insufficient spatial resolution

and spatial complexity, pixels in remotely sensed hyperspectral images are likely to be formed by a mixture of pure spectral constituents (endmembers) rather than a single substance [7]. Spectral unmixing, which estimates the fractional abundances of the pure spectral signatures or endmembers in each mixed pixel, was proposed to deal with the mixing problem [8].

For the past years, spectral unmixing has been one of the most active research lines in order to deal with mixed pixels, where traditional methods generally consist of two steps: endmember extraction and abundance inversion [7]. Under the linear mixture model, a group of unmixing approaches has been proposed, including geometric methods [9]–[12] and statistical methods [13]–[16]. These methods, which extract the endmembers directly from the scene, often encounter problems when generating spectral signatures without real physical meaning. With the wide availability of spectral libraries, sparse unmixing [17], as a semisupervised approach in which mixed pixels are expressed in the form of combinations of a number of pure spectral signatures from a large spectral library, is able to handle the drawbacks introduced by such *virtual* endmembers. In order to find an optimal subset of endmembers to represent the pixels in a hyperspectral image, sparse regression techniques have been proposed and exhibit significant advantages over unsupervised approaches [18]–[22].

In order to improve the unmixing results, a recent trend is to exploit the spatial contextual information [23]. Due to the spatial arrangement of the pixels in an image, their corresponding abundances often show a pronounced spatial dependence. In other words, hyperspectral images exhibit rich spatial information, and such valuable information can be of great benefit for estimating endmember abundances, and also make the obtained abundances more consistent [23]. The methods incorporating spatial information generally assume that the hyperspectral image consists of homogenous regions [24]–[28], and the corresponding abundances therefore are piecewise smooth [29], [30]. This uniform smoothness assumption implies that smooth abundance transitions happen everywhere in the scene [29]. However, in real scenarios, such homogeneity in the image does not lead to straightforward smoothness in the abundances. That is, although neighboring pixels likely share the same endmembers, their abundances are often expected to be different from each other. Specifically, hyperspectral data are often characterized by low spatial resolution and high spectral resolution. As a result, endmember abundances are expected to exhibit spatial discontinuities [31].

Manuscript received August 11, 2016; revised May 7, 2017 and August 4, 2017; accepted March 18, 2018. Date of publication May 16, 2018; date of current version September 25, 2018. This work was supported in part by the National Natural Science Foundation of China under Grant 61771496 and Grant 61362036, in part by the National Key Research and Development Program of China under Grant 2017YFB0502900, in part by the Guangdong Provincial Natural Science Foundation under Grant 2016A030313254, in part by the Open Research Fund of Jiangxi Province Key Laboratory of Water Information Cooperative Sensing and Intelligent Processing under Grant 2016WICSIP010, and in part by the Natural Science Foundation of Jiangxi China under Grant 20161BAB202040. (*Corresponding author: Jun Li.*)

S. Zhang and J. Li are with the Guangdong Provincial Key Laboratory of Urbanization and Geo-simulation, Center of Integrated Geographic Information Analysis, School of Geography and Planning, Sun Yat-sen University, Guangzhou 510275, China (e-mail: lijun48@mail.sysu.edu.cn).

Z. Wu is with the School of Computer Science and Engineering, Nanjing University of Science and Technology, Nanjing 210094, China, and also with the Jiangsu High Technology Research Key Laboratory for Wireless Sensor Networks, Nanjing 210003, China.

A. Plaza is with the Hyperspectral Computing Laboratory, Department of Technology of Computers and Communications, Escuela Politécnica, University of Extremadura, E-10003 Cáceres, Spain.

Color versions of one or more of the figures in this paper are available online at <http://ieeexplore.ieee.org>.

Digital Object Identifier 10.1109/TGRS.2018.2825457

Moreover, abrupt abundance changes are similar to region edges in image segmentation, which are known to happen naturally in remotely sensed scenes [32]. Therefore, it is necessary to develop new strategies to preserve the discontinuities in abundance maps for improving spectral unmixing.

In this paper, we develop a new spatial discontinuity-weighted sparse unmixing approach for hyperspectral images, which aims at smoothing the textures while preserving sharp edges in abundance estimation. Assuming that abundance maps are discontinuous, especially in the object boundaries, the proposed approach introduces a spatial relaxation technique to accurately preserve the edges in these maps. In the proposed approach, the edge information (detected by a Sobel operator) is used to characterize the discontinuities of the abundance maps. As demonstrated by our experimental results with both synthetic and real hyperspectral data sets, the proposed strategy can preserve the heterogeneity of abundance maps by including edge information into the sparse unmixing process.

The remainder of this paper is organized as follows. In Section II, we review the sparse unmixing theory. The proposed spatial discontinuity-weighted sparse unmixing is presented in Section III. Section IV describes our experimental results with simulated hyperspectral data sets. Section V describes experiments with real hyperspectral data. Finally, Section VI draws some conclusions and hints at plausible future research lines.

## II. SPARSE UNMIXING

Let  $\mathbf{Y} = [\mathbf{y}_1, \dots, \mathbf{y}_n] \in \mathbb{R}^{d \times n}$  denote a hyperspectral image, where  $n$  is the number of pixel vectors and  $d$  is the number of bands. Let  $\mathbf{A} \in \mathbb{R}^{d \times m}$  be a large spectral library, where  $m$  is the number of spectral signatures in  $\mathbf{A}$ , and  $\mathbf{X} = [\mathbf{x}_1, \dots, \mathbf{x}_n]$  denotes the abundance maps corresponding to library  $\mathbf{A}$  for the observed data  $\mathbf{Y}$ . With the aforementioned definitions in mind, sparse unmixing finds a linear combination of endmembers for  $\mathbf{Y}$  from the spectral library  $\mathbf{A}$

$$\mathbf{Y} = \mathbf{A}\mathbf{X} + \mathbf{N} \quad \text{s.t.: } \mathbf{X} \geq 0, \mathbf{1}^T \mathbf{x} = 1 \quad (1)$$

where  $\mathbf{N} \in \mathbb{R}^{d \times n}$  is the error,  $\mathbf{X} \geq 0$  is the so-called abundance nonnegativity constraint (ANC), and  $\mathbf{1}^T \mathbf{x} = 1$  is the abundance sum-to-one constraint (ASC). It should be noted that we explicitly enforce the ANC constraint without the ASC constraint due to some criticisms about the ASC in the literature [17].

As the number of endmembers involved in a mixed pixel is usually very small when compared with the size of the spectral library, the vector of fractional abundances  $\mathbf{X}$  is sparse. With these considerations in mind, the unmixing problem can be formulated as an  $\ell_2 - \ell_0$  optimization problem

$$\min_{\mathbf{X}} \frac{1}{2} \|\mathbf{A}\mathbf{X} - \mathbf{Y}\|_F^2 + \lambda \|\mathbf{X}\|_0 \quad \text{s.t.: } \mathbf{X} \geq 0 \quad (2)$$

where  $\|\cdot\|_F$  is the Frobenius norm and  $\lambda$  is a regularization parameter. Problem (2) is nonconvex and difficult to solve [33], [34]. The sparse unmixing algorithm via variable splitting and augmented Lagrangian (SUnSAL) alternatively uses the  $\ell_2 - \ell_1$

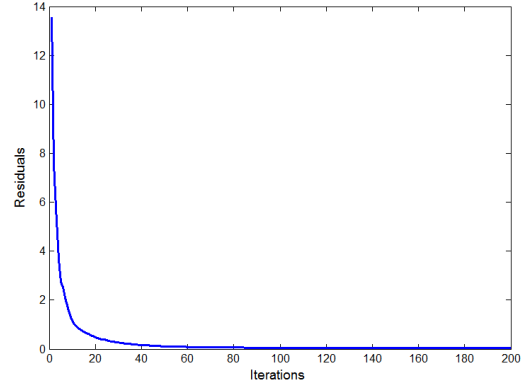


Fig. 1. Residual  $\|\mathbf{G}\mathbf{U}^{(j)} + \mathbf{B}\mathbf{V}^{(j)}\|_F$  as a function of the number of iterations for the complete algorithm.

norm to replace the  $\ell_2 - \ell_0$  norm and solve the unmixing problem as follows [35]:

$$\min_{\mathbf{X}} \frac{1}{2} \|\mathbf{A}\mathbf{X} - \mathbf{Y}\|_F^2 + \lambda \|\mathbf{X}\|_{1,1} \quad \text{s.t.: } \mathbf{X} \geq 0 \quad (3)$$

where  $\|\mathbf{X}\|_{1,1} = \sum_{j=1}^n \|\mathbf{x}_j\|_1$  with  $\mathbf{x}_j$  being the  $j$ th column of  $\mathbf{X}$ . SUnSAL solves the optimization problem in (3) efficiently using the alternative direction method of multipliers (ADMM) [35].

Similar to (3), in [36], an  $\ell_{2,1}$  mixed norm (called collaborative regularization) was proposed, which globally imposes sparsity among the endmembers in collaborative fashion for all pixels. According to the collaborative sparse unmixing model described in [36], the objective function can be defined as follows:

$$\min_{\mathbf{X}} \frac{1}{2} \|\mathbf{A}\mathbf{X} - \mathbf{Y}\|_F^2 + \lambda \sum_{k=1}^m \|\mathbf{x}^k\|_2 \quad \text{s.t. } \mathbf{x} \geq 0 \quad (4)$$

where  $\mathbf{x}^k$  denotes the  $k$ th line of  $\mathbf{X}$  ( $k = 1, 2, \dots, m$ ) and  $\sum_{k=1}^m \|\mathbf{x}^k\|_2$  is the so-called  $\ell_{2,1}$  mixed norm. Note that the main difference between SUnSAL and CLSUnSAL is that the former employs pixelwise independent regressions, while the latter enforces joint sparsity among all the pixels.

In order to take into account the spatial information of the image, a total variation (TV) regularizer can be integrated with SUnSAL (called SUnSAL-TV) to promote spatial homogeneity among neighboring pixels [29]

$$\min_{\mathbf{X}} \frac{1}{2} \|\mathbf{A}\mathbf{X} - \mathbf{Y}\|_F^2 + \lambda \|\mathbf{X}\|_{1,1} + \lambda_{TV} TV(\mathbf{X}) \quad \text{s.t.: } \mathbf{X} \geq 0 \quad (5)$$

where  $TV(\mathbf{X}) \equiv \sum_{i,j \in \varepsilon} \|\mathbf{x}_i - \mathbf{x}_j\|_1$ ,  $\varepsilon$  represents the set of (horizontal and vertical) pixel neighbors in the image, and  $\mathbf{x}_j$  denotes as a series of the neighboring pixels of  $\mathbf{x}_i$  in the abundance matrix  $\mathbf{X}$ . SUnSAL-TV shows a great potential to exploit the spatial information for sparse unmixing. However, it may lead to oversmoothness and blurred boundaries. Furthermore, in real scenarios, fractional abundances exhibit differences among neighboring pixels and sharp transitions (especially in the object boundaries). Based on this, in the following, we will present a discontinuity-preserving method to address this issue.

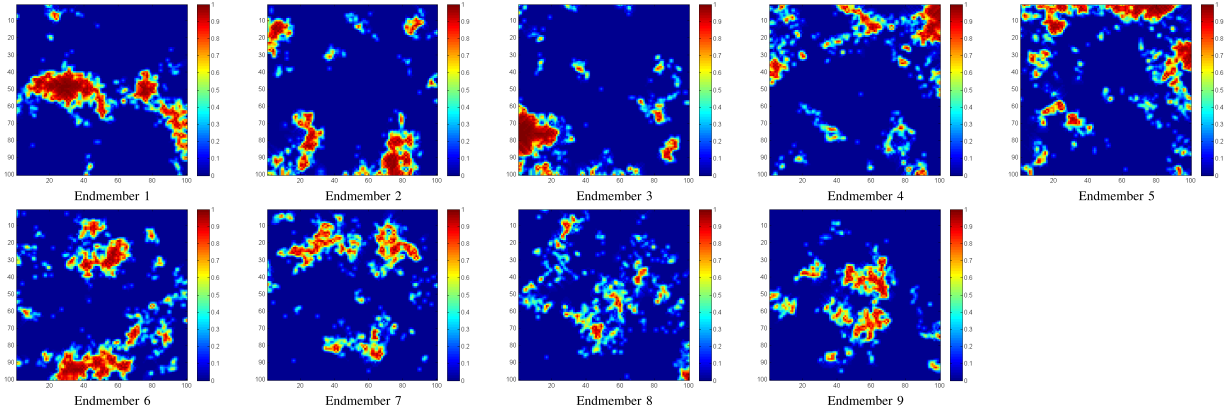


Fig. 2. True fractional abundances of the endmembers in the simulated DC1.

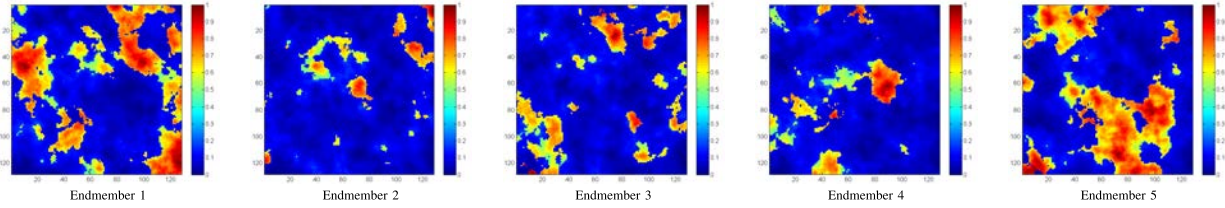


Fig. 3. True fractional abundances of the endmembers in the simulated DC2.

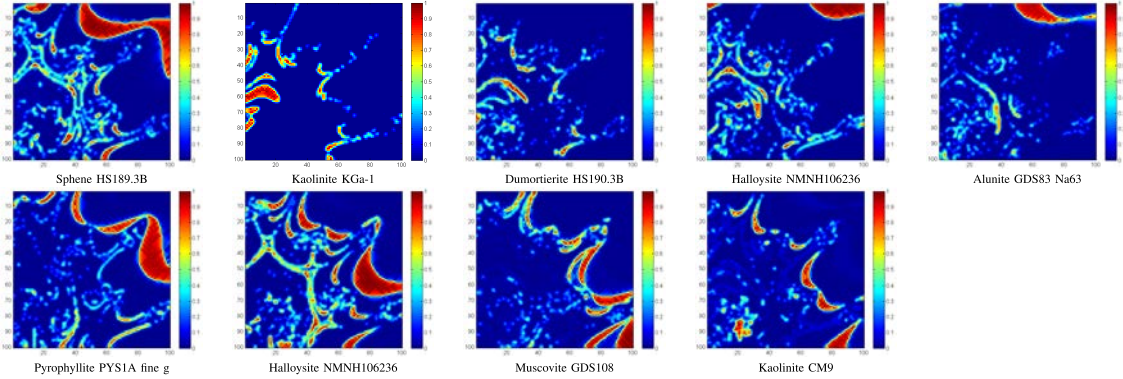


Fig. 4. True fractional abundances of the endmembers in the simulated DC3.

### III. SPATIAL DISCONTINUITY-WEIGHTED SPARSE UNMIXING

In this paper, we introduce a spatial discontinuity-preserving strategy for sparse unmixing. The proposed approach characterizes spatial edges through the inclusion of a discontinuity weight on the sparse regularizers. This weight aims at smoothing the textures while retaining sharp edges in the estimated abundances. Let  $\mathbf{X}^k$  denote the  $k$ th abundance map of  $\mathbf{X}$  and  $\zeta^k$  be the edge image of  $\mathbf{X}^k$  which is given by

$$\zeta^k = \exp(-\text{sobel}(\mathbf{X}^k)) \quad (6)$$

where  $\text{sobel}(\cdot)$  denotes the Sobel filter, which detects the discontinuities in  $\mathbf{X}^k$  and the output at each pixel is 0 or 1. In addition, to have a better interpretation of the edges, we considered the results obtained by applying  $\text{sobel}(\cdot)$  in both the vertical and horizontal directions. It should be noted that, in the literature, there are many approaches that have been developed for detecting edges, which can be divided into two categories. The Prewitt filter [37], Roberts filter [38],

and the mentioned Sobel filter are one order edge detection operators, while the Laplace filter [39] and Canny filter [40] are two order edge detection operators. All of these approaches can be considered as alternatives to the Sobel filter in (6). In this paper, we use the Sobel filter to detect the edges (spatial discontinuities) for two reasons. First of all, instead of comparing different edge detection algorithms, our goal in this paper is to exploit the spatial discontinuity information in sparse unmixing. As a result, the selection of the Sobel filter (a classic edge detection approach) seems a natural choice. Furthermore, we have empirically found that the Sobel filter generally provides very good edge detection results in different circumstances, which is consistent with the observations in other related research works [41]. For completeness, we report experiments in this paper that indicate that the Sobel edge detection operator can achieve better results than other edge detection operators.

Let  $\mathbf{v} = [\zeta^1, \dots, \zeta^m]^T$  be the edge images, extracted using (6). We would like to recall that  $m$  is the number of spectral signatures in the spectral library  $\mathbf{A}$ .

As aforementioned, the aim of this paper is to include the edge information in (6) for sparse unmixing purposes with the following two main goals. On the one hand, we aim at including the spatial information into sparse unmixing. On the other hand, we intend to avoid oversmoothness and blurring by preserving discontinuities in the abundance maps. To achieve this, we incorporate the edge information into the sparse regularizers in the sparse unmixing model. At this point, we emphasize that the proposed approach is a completely new framework, which can be plugged into any sparse unmixing model. As an example, in this paper, we introduce the edge image  $\mathbf{v}$  into the SUnSAL, CLSUnSAL, and SUnSAL-TV, leading to the following three algorithms that are denoted as follows.

1) *SUnSAL-DP*:

$$\min_{\mathbf{X}} \frac{1}{2} \|\mathbf{AX} - \mathbf{Y}\|_F^2 + \lambda \|\mathbf{v} \odot \mathbf{X}\|_{1,1} \quad \text{s.t.: } \mathbf{X} \geq 0 \quad (7)$$

where the operator  $\odot$  denotes the elementwise multiplication of two variables and the DP denotes the discontinuity-preserving strategy.

2) *CLSUnSAL-DP*:

$$\min_{\mathbf{X}} \frac{1}{2} \|\mathbf{AX} - \mathbf{Y}\|_F^2 + \lambda \|\mathbf{v} \odot \mathbf{X}\|_{2,1} \quad \text{s.t.: } \mathbf{X} \geq 0. \quad (8)$$

3) *SUnSAL-TV-DP*:

$$\min_{\mathbf{X}} \frac{1}{2} \|\mathbf{AX} - \mathbf{Y}\|_F^2 + \lambda \|\mathbf{v} \odot \mathbf{X}\|_{1,1} + \lambda_{TV} (\mathbf{v} \odot TV(\mathbf{X})) \quad \text{s.t.: } \mathbf{X} \geq 0. \quad (9)$$

Note that, as shown in (7)–(9), the edge information is plugged into the sparse unmixing model as a weight matrix. Following [17], [29], and [36], we can adopt the ADMM to solve these optimization problems. Given SUnSAL-DP in problem (7) as an example, in the following, we revisit the optimization in detail.

Let  $\mathcal{L}(\mathbf{U}, \mathbf{V}, \mathbf{D}) \equiv g(\mathbf{U}, \mathbf{V}) + (\mu/2) \|\mathbf{GU} + \mathbf{BV} - \mathbf{D}\|_F^2$  be the augmented Lagrangian for

$$\min_{\mathbf{U}, \mathbf{V}} g(\mathbf{V}) \quad \text{s.t.: } \mathbf{GU} + \mathbf{BV} = \mathbf{0}$$

where  $\mu > 0$  is a positive constant,  $\mathbf{U} = \mathbf{X}$ , and  $\mathbf{D} = (\mathbf{D}_1, \mathbf{D}_2, \mathbf{D}_3)$  denote the Lagrange multipliers associated with the constraint  $\mathbf{GU} + \mathbf{BV} = \mathbf{0}$ ;  $\mathbf{V} \equiv (\mathbf{V}_1, \mathbf{V}_2, \mathbf{V}_3)$ ,  $\mathbf{G} = [\mathbf{A}, \mathbf{I}, \mathbf{I}]^T$ , and  $\mathbf{B} = \text{diag}(-\mathbf{I})$ ;  $g(\mathbf{V}) \equiv (1/2) \|\mathbf{V}_1 - \mathbf{Y}\|_F^2 + \lambda \|\mathbf{v} \odot \mathbf{V}_2\|_{1,1} + \iota_{R_+}(\mathbf{V}_3)$  is the cost function of the following optimization problem:

$$\min_{\mathbf{U}, \mathbf{V}_1, \mathbf{V}_2, \mathbf{V}_3} \frac{1}{2} \|\mathbf{V}_1 - \mathbf{Y}\|_F^2 + \lambda \|\mathbf{v} \odot \mathbf{V}_2\|_{1,1} + \iota_{R_+}(\mathbf{V}_3) \quad \text{s.t. } \mathbf{V}_1 = \mathbf{AU}, \mathbf{V}_2 = \mathbf{U}, \mathbf{V}_3 = \mathbf{U} \quad (10)$$

where  $\iota_{R_+}(\mathbf{X}) = \sum_{i=1}^n \iota_{R_+}(\mathbf{x}_i)$  is the indicator function, and  $\iota_{R_+}(\mathbf{x}_i)$  is zero if  $\mathbf{x}_i$  belongs to the nonnegative orthant and  $+\infty$  otherwise.

Now, we can implement the ADMM to solve the optimization problem involved in SUnSAL-DP, as shown in Algorithm 1. In practical implementations, the algorithm stops when the maximum iteration number is reached or  $\|\mathbf{GU}^{(j)} + \mathbf{BV}^{(j)}\|_F \leq \text{threshold}$ .

---

### Algorithm 1 Pseudocode of the SUnSAL-DP Algorithm

---

1: **Initialization:**

2: set  $k, j = 0$ , choose  $\mu > 0$ ,  $\mathbf{U}^{(0)}, \mathbf{V}_1^{(0)}, \mathbf{V}_2^{(0)}, \mathbf{V}_3^{(0)}, \mathbf{D}_1^{(0)}, \mathbf{D}_2^{(0)}, \mathbf{D}_3^{(0)}$

3: **Repeat:**

4:  $\mathbf{v}^{(j)} \leftarrow \exp(-\text{sobel}(\mathbf{U}^{(j)}))$

5: **Repeat:**

6:  $\mathbf{U}^{(k+1)} \leftarrow (\mathbf{A}^T \mathbf{A} + 2\mathbf{I})^{-1} (\mathbf{A}^T (\mathbf{V}_1^{(k)} + \mathbf{D}_1^{(k)}) + \mathbf{V}_2^{(k)} + \mathbf{D}_2^{(k)} + \mathbf{V}_3^{(k)} + \mathbf{D}_3^{(k)})$

7:  $\mathbf{V}_1^{(k+1)} \leftarrow \frac{1}{1+\mu} [\mathbf{Y} + \mu (\mathbf{AU}^{(k+1)} - \mathbf{D}_1^{(k)})]$

8:  $\mathbf{V}_2^{(k+1)} \leftarrow \text{soft}(\mathbf{U}^{(k+1)} - \mathbf{D}_2^{(k)}, \frac{2}{\mu} \mathbf{v}^{(j)})$

9:  $\mathbf{V}_3^{(k+1)} \leftarrow \max(\mathbf{U}^{(k+1)} - \mathbf{D}_3^{(k)}, 0)$

10: **Update Lagrange multipliers:**

11:  $\mathbf{D}_1^{(k+1)} \leftarrow \mathbf{D}_1^{(k)} - \mathbf{AU}^{(k+1)} + \mathbf{V}_1^{(k+1)}$

12:  $\mathbf{D}_2^{(k+1)} \leftarrow \mathbf{D}_2^{(k)} - \mathbf{U}^{(k+1)} + \mathbf{V}_2^{(k+1)}$

13:  $\mathbf{D}_3^{(k+1)} \leftarrow \mathbf{D}_3^{(k)} - \mathbf{U}^{(k+1)} + \mathbf{V}_3^{(k+1)}$

14: **Update iteration:**  $k \leftarrow k + 1$

15:  $\mathbf{U}^{(j+1)} \leftarrow \mathbf{U}^{(k+1)}$

16: **Update iteration:**  $j \leftarrow j + 1$

17: **until** some stopping criterion is satisfied.

---

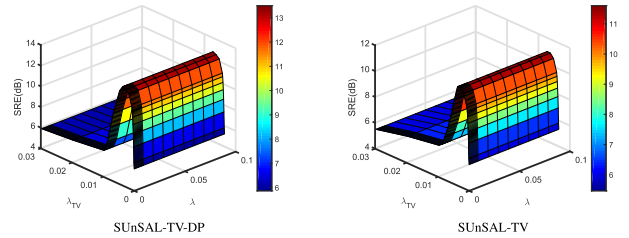


Fig. 5. SRE (dB) as a function of parameters  $\lambda$  and  $\lambda_{TV}$  for DC1 with SNR = 30 dB.

It should be noted that, in each ADMM, the weight matrix  $\mathbf{v}$  (i.e., edge information) is computed beforehand. In practice, we empirically find out that each ADMM converges in a few iterations, i.e., less than five iterations. Furthermore, Fig. 1 shows the obtained residual, i.e.,  $\|\mathbf{GU}^{(j)} + \mathbf{BV}^{(j)}\|_F$ , as the function of the number of iterations for the complete algorithm. It can be observed that the full scheme also converges very fast. Therefore, in our experiments performed in this paper, the number of iterations involved in the ADMM  $k$  and that in the DP  $j$  are set to 5 and 200, respectively. Finally, note that the frameworks proposed in (7)–(9) open the door to include spatial information via a weight matrix, which can be adapted to many forms, such as superpixel information [42]–[44], local neighboring pixels [45]–[48], and nonlocal information [49], [50]. Nevertheless, in this paper, the spatial weight matrix is defined by the edge information due to our focus on preserving discontinuities.

## IV. EXPERIMENTS WITH SYNTHETIC DATA

In this section, we illustrate the unmixing performance of the proposed discontinuity-weighted sparse unmixing method using simulated hyperspectral data sets.

For quantitative analysis, the signal-to-reconstruction error (SRE), measured in dB, is used to evaluate the unmixing

TABLE I

SRE (dB),  $p_s$ , AND *Sparsity* SCORES ACHIEVED AFTER APPLYING DIFFERENT UNMIXING METHODS TO THE SIMULATED DC1 (THE OPTIMAL PARAMETERS FOR WHICH THE REPORTED VALUES WERE ACHIEVED ARE INDICATED IN THE PARENTHESES)

Algorithm	SNR=30dB			SNR=40dB			SNR=50dB		
	SRE(dB)	$p_s$	<i>sparsity</i>	SRE(dB)	$p_s$	<i>sparsity</i>	SRE(dB)	$p_s$	<i>sparsity</i>
SUnSAL	8.4007	0.7905	0.0497	15.1565	0.9882	0.0426	23.1321	1	0.0257
	$(\lambda = 2e-2)$			$(\lambda = 4e-3)$			$(\lambda = 1e-3)$		
SUnSAL-DP	10.1799	0.8929	0.0424	16.3913	0.9933	0.0373	24.6139	1	0.0208
	$(\lambda = 2e-2)$			$(\lambda = 4e-3)$			$(\lambda = 1e-3)$		
CLSunSAL	6.8737	0.7519	0.0931	15.3188	0.9915	0.0604	26.0032	1	0.0153
	$(\lambda = 3e-1)$			$(\lambda = 3e-2)$			$(\lambda = 2e-2)$		
CLSunSAL-DP	8.0734	0.8307	0.0841	17.0520	0.9996	0.0553	26.1533	1	0.0141
	$(\lambda = 3e-1)$			$(\lambda = 3e-2)$			$(\lambda = 2e-2)$		
SUnSAL-TV	11.5332	0.9608	0.0552	17.8147	0.9999	0.0341	26.1521	1	0.0178
	$(\lambda = 1e-2; \lambda_{TV} = 4e-3)$			$(\lambda = 5e-3; \lambda_{TV} = 1e-3)$			$(\lambda = 2e-3; \lambda_{TV} = 2e-4)$		
SUnSAL-TV-DP	13.4972	0.9802	0.0391	20.4687	1	0.0222	27.4673	1	0.0142
	$(\lambda = 1e-2; \lambda_{TV} = 4e-3)$			$(\lambda = 5e-3; \lambda_{TV} = 1e-3)$			$(\lambda = 2e-3; \lambda_{TV} = 2e-4)$		

TABLE II

SRE (dB),  $p_s$ , AND *Sparsity* SCORES ACHIEVED AFTER APPLYING DIFFERENT UNMIXING METHODS TO THE SIMULATED DC2 (THE OPTIMAL PARAMETERS FOR WHICH THE REPORTED VALUES WERE ACHIEVED ARE INDICATED IN THE PARENTHESES)

Algorithm	SNR=30dB			SNR=40dB			SNR=50dB		
	SRE(dB)	$p_s$	<i>sparsity</i>	SRE(dB)	$p_s$	<i>sparsity</i>	SRE(dB)	$p_s$	<i>sparsity</i>
SUnSAL	8.7002	0.9036	0.0546	15.2436	0.9999	0.0520	23.0201	1	0.0325
	$(\lambda = 3e-2)$			$(\lambda = 7e-3)$			$(\lambda = 2e-3)$		
SUnSAL-DP	10.2049	0.9351	0.0493	15.6721	1	0.0478	23.6568	1	0.0313
	$(\lambda = 3e-2)$			$(\lambda = 7e-3)$			$(\lambda = 2e-3)$		
CLSunSAL	10.2840	0.9948	0.0860	19.7746	1	0.0291	29.2758	1	0.0208
	$(\lambda = 7e-1)$			$(\lambda = 3e-1)$			$(\lambda = 7e-2)$		
CLSunSAL-DP	11.5258	0.9961	0.0796	20.7879	1	0.0247	30.7346	1	0.0207
	$(\lambda = 7e-1)$			$(\lambda = 3e-1)$			$(\lambda = 7e-2)$		
SUnSAL-TV	15.0700	0.9957	0.0506	22.9806	1	0.0266	32.4023	1	0.0210
	$(\lambda = 1e-3; \lambda_{TV} = 8e-3)$			$(\lambda = 1e-3; \lambda_{TV} = 3e-3)$			$(\lambda = 8e-4; \lambda_{TV} = 5e-4)$		
SUnSAL-TV-DP	16.1273	0.9963	0.0456	23.8661	1	0.0234	33.4405	1	0.0208
	$(\lambda = 1e-3; \lambda_{TV} = 8e-3)$			$(\lambda = 1e-3; \lambda_{TV} = 3e-3)$			$(\lambda = 8e-4; \lambda_{TV} = 5e-4)$		

accuracy. Let  $\hat{\mathbf{x}}$  be the estimated abundance, and  $\mathbf{x}$  be the true abundance. The SRE (dB) can be computed as follows:

$$\text{SRE(dB)} = 10 \cdot \log_{10} (E(\|\mathbf{x}\|_2^2) / E(\|\mathbf{x} - \hat{\mathbf{x}}\|_2^2)) \quad (11)$$

where  $E(\cdot)$  denotes the expectation function. It should be noted that the larger the SRE (dB) is, the more accurate the unmixing is.

For further analysis, we use another indicator, i.e., the ‘‘probability of success,’’  $p_s$ , which is an estimate of the probability that the relative error power is smaller than a certain threshold. It is formally defined as follows:  $p_s \equiv P(\|\hat{\mathbf{x}} - \mathbf{x}\|^2 / \|\mathbf{x}\|^2 \leq \text{threshold})$ . For example, if we set threshold = 10 and get  $p_s = 1$ , this means that the total relative error power of the fractional abundances is, with probability 1, less than 1/10. This gives an indication about the stability of the estimation that cannot be directly derived from the SRE.

In our case, the estimation result is considered successfully when  $\|\hat{\mathbf{x}} - \mathbf{x}\|^2 / \|\mathbf{x}\|^2 \leq 3.16$  (5 dB). This threshold was demonstrated in [17]. Furthermore, the number of elements in  $\hat{\mathbf{x}}$  that is greater than 0.005 is counted; their proportion in all elements of the abundance matrix is defined as *sparsity*. The smaller the *sparsity* is, the more sparse the unmixing solution is.

#### A. Simulated Data Sets

Two spectral libraries are considered in our experiments, which are dictionaries of minerals extracted from the U.S. Geological Survey (USGS) library.<sup>1</sup> The first library  $\mathbf{A}_1$  contains  $m = 240$  materials (different mineral types), which comprises spectral signatures with reflectance values

<sup>1</sup>Available online at <http://speclab.cr.usgs.gov/spectral.lib06>.

TABLE III

SRE (dB),  $p_s$ , AND Sparsity SCORES ACHIEVED AFTER APPLYING DIFFERENT UNMIXING METHODS TO THE SIMULATED DC3 (THE OPTIMAL PARAMETERS FOR WHICH THE REPORTED VALUES WERE ACHIEVED ARE INDICATED IN THE PARENTHESES)

Algorithm	SNR=30dB			SNR=40dB			SNR=50dB		
	SRE(dB)	$p_s$	sparsity	SRE(dB)	$p_s$	sparsity	SRE(dB)	$p_s$	sparsity
SUnSAL	4.4136	0.6065	0.0609	7.7600	0.7914	0.0702	13.3519	0.9762	0.0505
	$(\lambda = 1e-2)$			$(\lambda = 5e-4)$			$(\lambda = 2e-4)$		
SUnSAL-DP	5.1223	0.6206	0.0565	8.8733	0.8051	0.0674	15.2979	0.9876	0.0447
	$(\lambda = 1e-2)$			$(\lambda = 5e-4)$			$(\lambda = 2e-4)$		
CLSunSAL	4.8296	0.6277	0.1181	9.5814	0.8985	0.1010	22.8229	1	0.0333
	$(\lambda = 2e-1)$			$(\lambda = 9e-3)$			$(\lambda = 7e-3)$		
CLSunSAL-DP	5.2377	0.6611	0.1114	10.8164	0.9567	0.0979	24.7669	1	0.0277
	$(\lambda = 2e-1)$			$(\lambda = 9e-3)$			$(\lambda = 7e-3)$		
SUnSAL-TV	6.2483	0.6282	0.1094	11.6088	0.9045	0.0867	21.3122	1	0.0434
	$(\lambda = 1e-7; \lambda_{TV} = 1e-3)$			$(\lambda = 1e-7; \lambda_{TV} = 3e-4)$			$(\lambda = 1e-7; \lambda_{TV} = 5e-5)$		
SUnSAL-TV-DP	6.7786	0.6649	0.1052	12.5137	0.9284	0.0806	22.4827	1	0.0410
	$(\lambda = 1e-7; \lambda_{TV} = 1e-3)$			$(\lambda = 1e-7; \lambda_{TV} = 3e-4)$			$(\lambda = 1e-7; \lambda_{TV} = 5e-5)$		

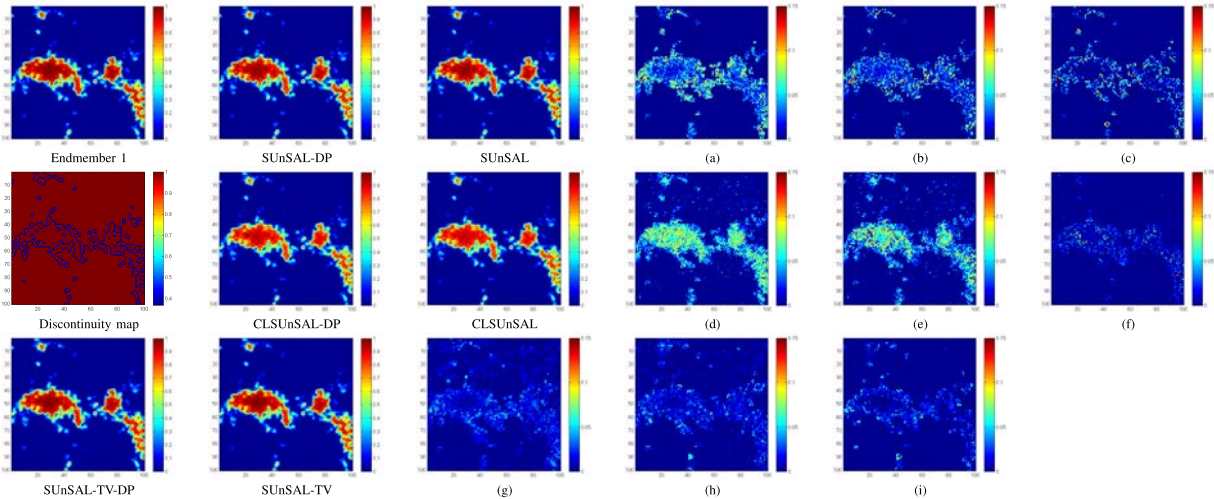


Fig. 6. Abundance maps obtained for the first endmember from DC1 under noise ratio of SNR = 40 dB. (a) Difference map between the ground-truth abundance and the result obtained by SUnSAL. (b) Difference map between the ground-truth abundance and the result obtained by SUnSAL-DP. (c) Difference map between the results obtained by SUnSAL-DP and SUnSAL. (d) Difference map between the ground-truth abundance and the result obtained by CLSunSAL. (e) Difference map between the ground-truth abundance and the result obtained by CLSunSAL-DP. (f) Difference map between the results obtained by CLSunSAL-DP and CLSunSAL. (g) Difference map between the ground-truth abundance and the result obtained by SUnSAL-TV-DP. (h) Difference map between the ground-truth abundance and the result obtained by SUnSAL-TV. (i) Difference map between the results obtained by SUnSAL-TV-DP and SUnSAL-TV.

given in  $L = 224$  spectral bands and distributed uniformly in the interval  $0.4\text{--}2.5 \mu\text{m}$ . The library  $\mathbf{A}_2$  contains  $m = 233$  materials (different mineral types), which comprises spectral signatures with reflectance values given in  $L = 221$  spectral bands and distributed uniformly in the interval  $0.4\text{--}2.5 \mu\text{m}$ . Three different data sets are simulated, in which the fractional abundances are subject to the ANC and ASC.

1) *Simulated Data Cube 1 (DC1)*: DC1 is generated with  $100 \times 100$  pixels and nine signatures, which are randomly chosen from the spectral library  $\mathbf{A}_1$ . The fractional abundances are piecewise smooth, i.e., they are smooth with sharp transitions, especially in the boundaries of image objects. These data can reveal the spatial features quite well for the different unmixing

algorithms. For illustrative purposes, Fig. 2 shows the true abundance maps of the endmembers. After generating the data cube, it was contaminated with independent identically distributed Gaussian noise for three levels of the signal-to-noise (SNR) ratio: 30, 40, and 50 dB.

2) *Simulated Data Cube 2 (DC2)*: This simulated data cube was generated using the Hyperspectral Imagery Synthesis toolbox for MATLAB, which was published by Computational Intelligence Group of Basque University.<sup>2</sup> It provides different options of creating synthetic images with spatial patterns and allows users to define spatial dimensions of the images as well as the number of

<sup>2</sup>[www.ehu.es/ccwintco/index.php/Hyperspectral\\_Imagery\\_Synthesis\\_tools\\_for\\_MATLAB](http://www.ehu.es/ccwintco/index.php/Hyperspectral_Imagery_Synthesis_tools_for_MATLAB).

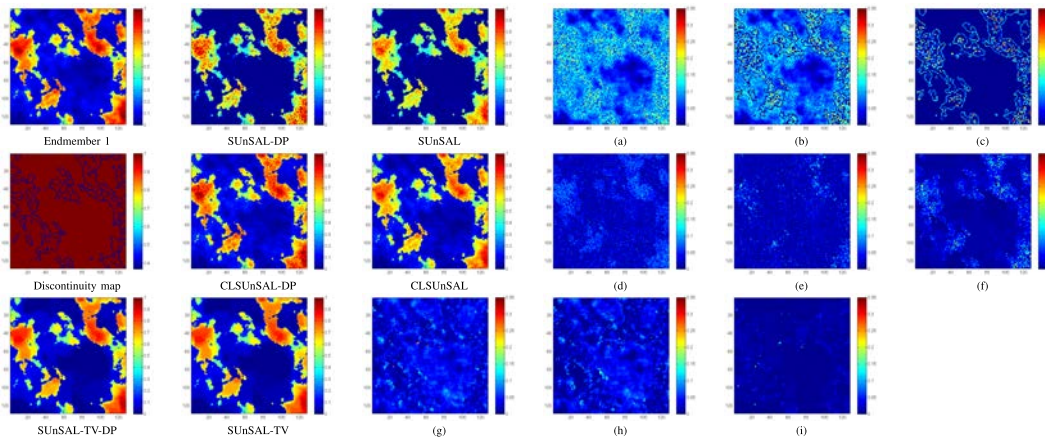


Fig. 7. Abundance maps obtained for the first endmember from DC2 under noise ratio of SNR = 40 dB. (a) Difference map between the ground-truth abundance and the result obtained by SUNSAL. (b) Difference map between the ground-truth abundance and the result obtained by SUNSAL-DP. (c) Difference map between the results obtained by SUNSAL-DP and SUNSAL. (d) Difference map between the ground-truth abundance and the result obtained by CLSUNSAL. (e) Difference map between the ground-truth abundance and the result obtained by CLSUNSAL-DP. (f) Difference map between the results obtained by CLSUNSAL-DP and CLSUNSAL. (g) Difference map between the ground-truth abundance and the result obtained by SUNSAL-TV. (h) Difference map between the ground-truth abundance and the result obtained by SUNSAL-TV-DP. (i) Difference map between the results obtained by SUNSAL-TV-DP and SUNSAL-TV.

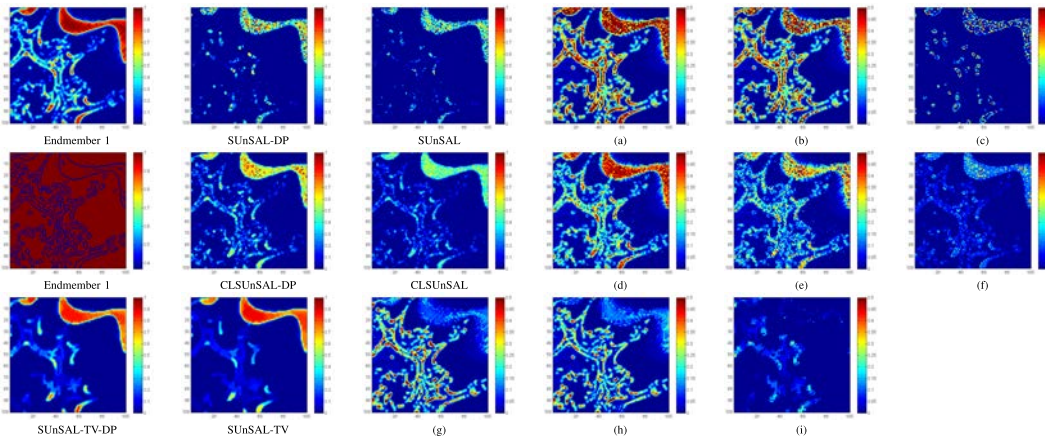


Fig. 8. Abundance maps obtained for the endmember *Sphene HS189.3B* from DC3 under noise ratio of SNR = 40 dB. (a) Difference map between the ground-truth abundance and the result obtained by SUNSAL. (b) Difference map between the ground-truth abundance and the result obtained by SUNSAL-DP. (c) Difference map between the results obtained by SUNSAL-DP and SUNSAL. (d) Difference map between the ground-truth abundance and the result obtained by CLSUNSAL. (e) Difference map between the ground-truth abundance and the result obtained by CLSUNSAL-DP. (f) Difference map between the results obtained by CLSUNSAL-DP and CLSUNSAL. (g) Difference map between the ground-truth abundance and the result obtained by SUNSAL-TV. (h) Difference map between the ground-truth abundance and the result obtained by SUNSAL-TV-DP. (i) Difference map between the results obtained by SUNSAL-TV-DP and SUNSAL-TV.

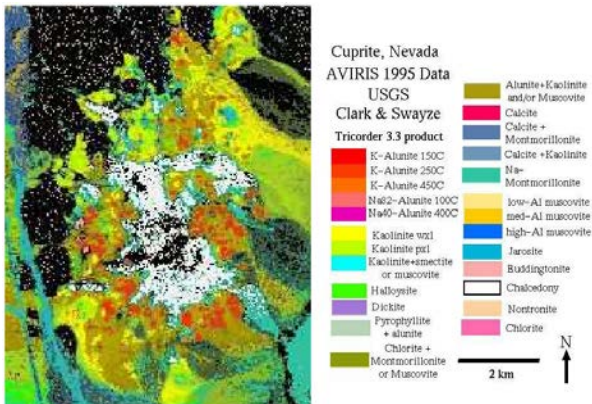


Fig. 9. USGS map showing the location of different minerals in the Cuprite mining district in Nevada.

endmembers utilized. The DC2 with a size of  $128 \times 128$  pixels was generated according to the Matern Gaussian field with the five endmembers, which were randomly

selected from  $A_1$ . The ground-truth fractional abundance maps for DC2 are shown in Fig. 3. Similar to DC1, the Gaussian noise with SNR = 30, 40, and 50 dB is included in the experiments.

3) *Simulated Data Cube 3 (DC3)*: Following the work in [24] and [25], a database of  $100 \times 100$  pixel synthetic hyperspectral scene has been created using fractals to generate distinct spatial patterns that are often found in nature. Nine spectral signatures are chosen from  $A_2$  to generate the synthetic hyperspectral images: Alunite GDS83 Na63, Dumortierite HS190.3B, Halloysite NMNH106236, Kaolinite CM9, Kaolinite KGa-1 (wxy1), Muscovite GDS108, Nontronite GDS41, Pyrophyllite PYS1A fine g, and Sphene HS189.3B are used to generate the synthetic hyperspectral images. The fractional abundance maps associated with each signature in the construction of the aforementioned synthetic scene are shown in Fig. 4. Similar to DC1 and DC2,

TABLE IV

SRE (dB),  $p_s$ , AND Sparsity SCORES ACHIEVED AFTER APPLYING DIFFERENT UNMIXING METHODS AND DIFFERENT EDGE DETECTION OPERATORS TO THE SIMULATED DC1 WITH AN SNR OF 30 dB (THE OPTIMAL PARAMETERS FOR WHICH THE REPORTED VALUES WERE ACHIEVED ARE INDICATED IN THE PARENTHESES)

Algorithm	SUnSAL-DP			CLSunSAL-DP			SUnSAL-TV-DP		
	SRE(dB)	$p_s$	sparsity	SRE(dB)	$p_s$	sparsity	SRE(dB)	$p_s$	sparsity
Sobel	10.1799	0.8929	0.0424	8.0734	0.8307	0.0841	13.4972	0.9802	0.0391
	$(\lambda = 2e-2)$			$(\lambda = 3e-1)$			$(\lambda = 1e-2; \lambda_{TV} = 4e-3)$		
Prewitt	9.8428	0.8756	0.0424	8.0627	0.8303	0.0851	13.3244	0.9751	0.0394
	$(\lambda = 2e-2)$			$(\lambda = 3e-1)$			$(\lambda = 1e-2; \lambda_{TV} = 4e-3)$		
Roberts	9.0468	0.8300	0.0450	7.9966	0.8204	0.0844	12.8861	0.9706	0.0400
	$(\lambda = 2e-2)$			$(\lambda = 3e-1)$			$(\lambda = 1e-2; \lambda_{TV} = 4e-3)$		
Laplacian	8.9299	0.8345	0.0453	7.5551	0.7956	0.0867	12.9087	0.9769	0.0429
	$(\lambda = 2e-2)$			$(\lambda = 3e-1)$			$(\lambda = 1e-2; \lambda_{TV} = 4e-3)$		
Canny	8.4885	0.7989	0.0496	6.9447	0.7542	0.0925	11.6087	0.9522	0.0519
	$(\lambda = 2e-2)$			$(\lambda = 3e-1)$			$(\lambda = 1e-2; \lambda_{TV} = 4e-3)$		

TABLE V

PER-ITERATION PROCESSING TIMES IN SECONDS TO PROCESS THE SIMULATED DC1 WITH AN SNR OF 40 dB

Algorithm	SUnSAL	SUnSAL-DP	CLSunSAL	CLSunSAL-DP	SUnSAL-TV	SUnSAL-TV-DP	MUSIC-CSR	MUSIC-CSR-DP
Time(s)	0.0814	0.3687	0.2695	0.5877	1.1125	2.1401	0.0101	0.0609

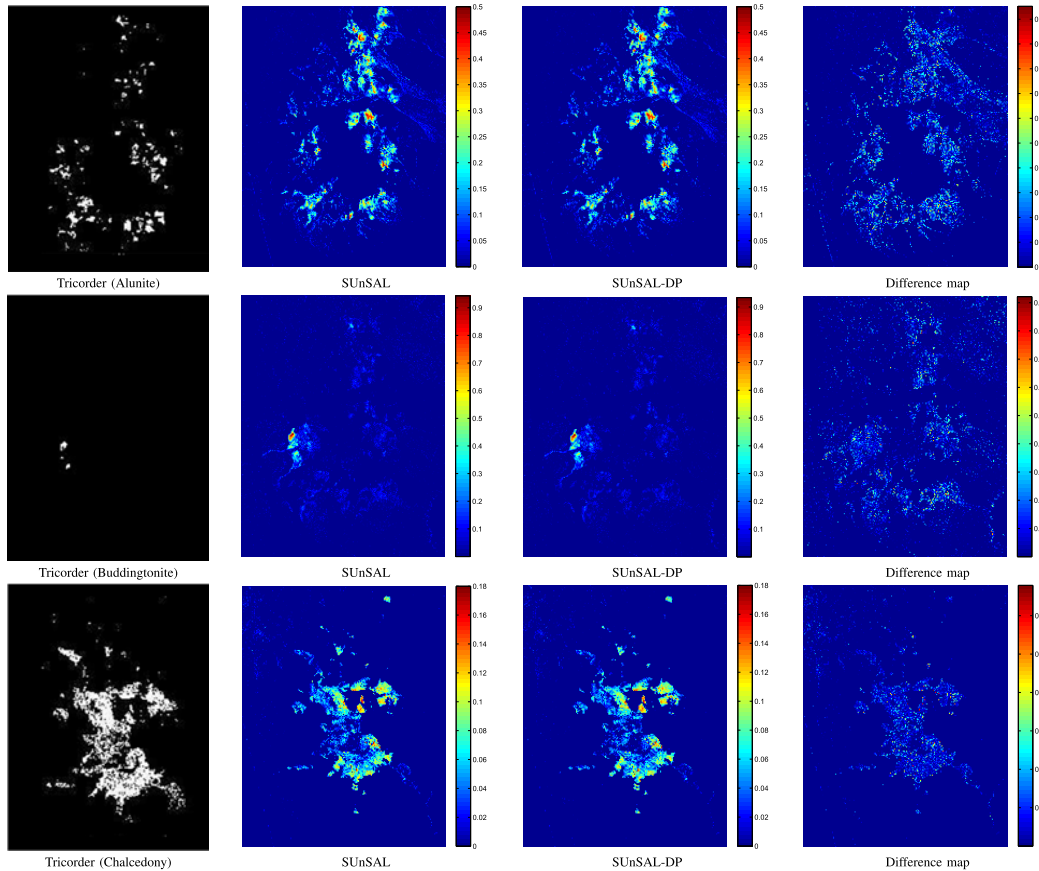


Fig. 10. Fractional abundance maps (Alunite HS295.3B, Buddingtonite GDS85 D-206, and Chalcedony CU91-6A) estimated by SUnSAL and SUnSAL-DP compared with the classification maps produced by USGS Tricorder software for the considered  $250 \times 191$  pixel subset of the AVIRIS Cuprite scene and the difference map between the results obtained by SUnSAL-DP and SUnSAL.

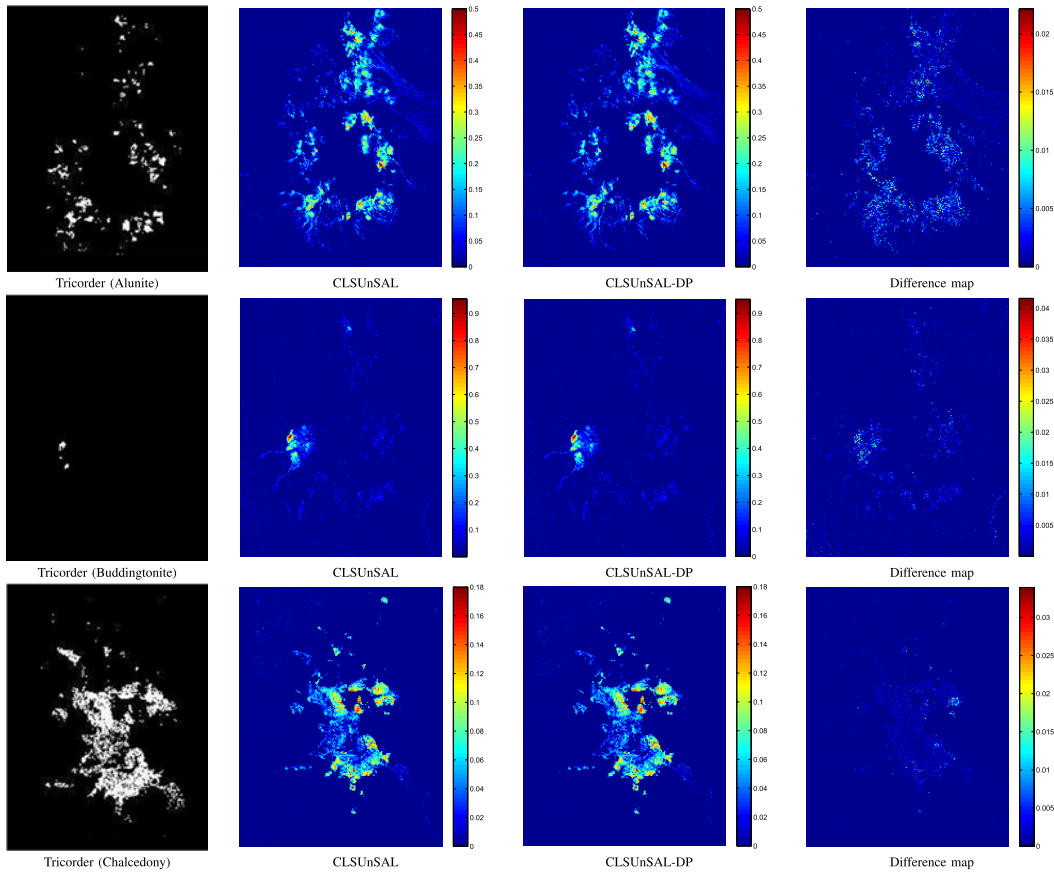


Fig. 11. Fractional abundance maps (Alunite HS295.3B, Buddingtonite GDS85 D-206, and Chalcedony CU91-6A) estimated by CLSUnSAL and CLSUnSAL-DP compared with the classification maps produced by USGS Tricorder software for the considered  $250 \times 191$  pixel subset of the AVIRIS Cuprite scene and the difference map between the results obtained by CLSUnSAL-DP and CLSUnSAL.

the Gaussian noise with SNR = 30, 40, and 50 dB is included in the experiments.

*B. Impact of the Regularization Parameters*

To analyze the impact of the regularization parameters involved in the considered methods (taking SUnSAL-TV-DP and SUnSAL-TV as an example), Fig. 5 shows the SRE (dB) values versus a series of different combinations of  $\lambda$  and  $\lambda_{TV}$  for DC1 with SNR = 30 dB. It can be observed that the proposed approach is consistent with the SUnSAL-TV method in terms of parameter selection, which reveals that there is no additional sensitivity from the DP viewpoint. Furthermore, it can be observed that, similar to SUnSAL-TV, the proposed approach performs well with a relative large range of options for the parameters. Finally, the results obtained by SUnSAL-TV-DP are better than those by SUnSAL-TV, which is expected as the proposed approach preserves the discontinuity.

*C. Results and Discussion*

We tested the performance of the proposed discontinuity-preserving strategy combined with sparse unmixing formulation using the three aforementioned simulated data cubes, DC1, DC2, and DC3, and compared the obtained results with those produced by the original SUnSAL, CLSUnSAL, and

SUnSAL-TV algorithms. Tables I–III show the SRE (dB),  $p_s$ , and *sparsity* results achieved by the different tested methods with the three considered simulated data sets using all considered SNR levels. In Tables I–III, the best scores obtained across the considered parameter range (the optimal parameters for which the reported values were obtained are indicated in the parentheses) were reported. From Tables I–III, we can see that the inclusion of the discontinuity-preserving strategy can improve the SREs in all the three considered scenarios. Furthermore, the advantage of the spatial discontinuity weight is even higher.  $p_s$  obtained by the proposed approaches is much better than that of SUnSAL, CLSUnSAL, and SUnSAL-TV in the case of low SNR, which reveals that the inclusion of spatial information leads to high robustness. In addition, the proposed approaches can result in a substantial *sparsity* performance improvement and can achieve more sparse results than SUnSAL, CLSUnSAL, and SUnSAL-TV. Actually, by including the edge information, it can improve the spatial *sparsity*. In addition, these experiments confirm the validity of the proposed method. Based on this, we can conclude that the inclusion of the spatial discontinuity-preserving strategy offers the potential to improve unmixing performance in three different analysis scenarios.

For illustrative purposes, Figs. 6–8 show a graphical comparison of the considered unmixing algorithms for the simulated problems with an SNR of 40 dB, in which only

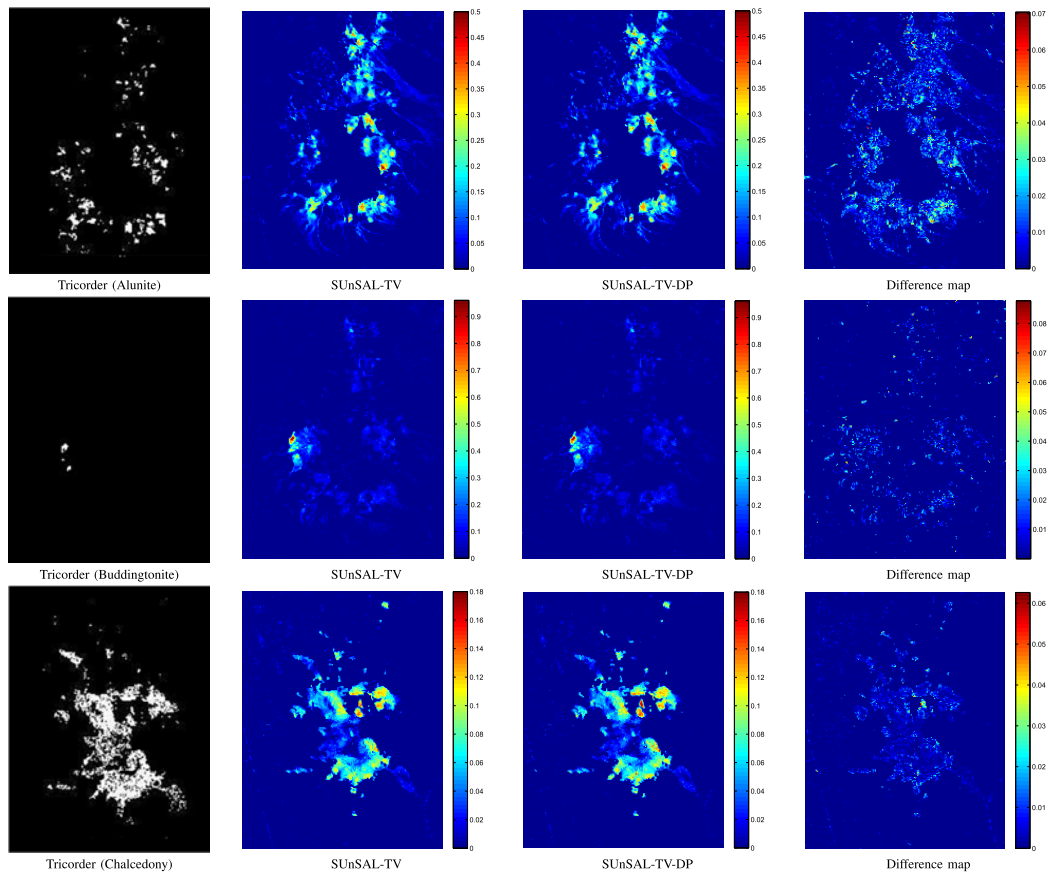


Fig. 12. Fractional abundance maps (Alunite HS295.3B, Buddingtonite GDS85 D-206, and Chalcedony CU91-6A) estimated by SUnSAL-TV and SUnSAL-TV-DP compared with the classification maps produced by USGS Tricorder software for the considered  $250 \times 191$  pixel subset of the AVIRIS Cuprite scene and the difference map between the results obtained by SUnSAL-TV-DP and SUnSAL-TV.

the abundance map of endmember 1 is presented, as the abundance maps estimated for all endmembers have exhibited a similar behavior. The difference maps between the estimated abundances and the real ones are also computed. From those difference maps, we can observe that the results produced by the proposed approach exhibit more details, especially along the discontinuous regions, as shown in the difference maps between the approach with and without the discontinuity weight.

To illustrate our selection of the Sobel edge detection operator, one order (including Prewitt and Roberts operators) and two order (including Laplacian and Canny operators) edge detection operators were used to compare with the Sobel edge detection operator. As shown in Table IV, the one order algorithms are better than the two order algorithms in most cases, and the Sobel operator has achieved the best results overall. This further explains why the Sobel edge detection operator can exploit the spatial discontinuity well for sparse unmixing. As a result, the selection of the Sobel filter seems a good choice in our context.

In order to evaluate the computational cost of the proposed discontinuity-preserving strategy, Table V reports the processing times for the DC1 with an SNR of 40 dB. All the algorithms were implemented using MATLAB R2012a on a desktop computer equipped with an Intel Core 7 Duo

central processing unit (at 3.6 GHz) and 32 GB of RAM memory. It can be observed that the proposed SUnSAL-DP, CLSUnSAL-DP, and SUnSAL-TV-DP are a bit slower than SUnSAL, CLSUnSAL, and SUnSAL-TV, respectively, due to the increased model complexity. Moreover, once the spectral library was pruned by multiple signal classification (MUSIC) [51] or robust MUSIC [52], the calculation speed will be faster. In addition, the MUSIC-CSR-DP is just a little slower than MUSIC-CSR. This suggests that the less the number of endmember in the spectral library is, the faster the computation speed is.

## V. EXPERIMENTS WITH REAL HYPERSPECTRAL DATA

In this section, we use the well-known Airborne Visible Infrared Imaging Spectrometer (AVIRIS) Cuprite data set for the evaluation of the proposed approach, which is available online in reflectance units.<sup>3</sup> The portion used in experiments corresponds to a  $250 \times 191$  pixel subset of the scene with 224 spectral bands in the range  $0.4\text{--}2.5 \mu\text{m}$  and the nominal spectral resolution of 10 nm. Prior to the analysis, bands 1–2, 105–115, 150–170, and 223–224 were removed due to water absorption and low SNR, leaving a total of 188 spectral bands. The spectral library used in this experiment is the

<sup>3</sup><http://aviris.jpl.nasa.gov/html/aviris.freedata.html>.

library  $\mathbf{A}_1$  used in the first two simulated experiments and the corresponding noisy bands are also removed from  $\mathbf{A}_1$ . For illustrative purposes, Fig. 9 shows a mineral map produced in 1995 by USGS, in which the Tricorder 3.3 software product [53] was used to map different minerals present in the Cuprite mining district. The USGS map serves as a good indicator for qualitative assessment of the fractional abundance maps produced by the different unmixing algorithms. Note that the publicly available AVIRIS Cuprite data were collected in 1997, but the Tricorder map was produced in 1995. Thus, we can only make a qualitative analysis of the performances of different sparse unmixing algorithms by comparing their estimated abundances with the mineral map.

Figs. 10–12 conduct a qualitative comparison between the classification maps produced by the USGS Tricorder software and the fractional abundances estimated by SUnSAL, SUnSAL-DP, CLSUnSAL, CLSUnSAL-DP, SUnSAL-TV, and SUnSAL-TV-DP algorithms for three highly representative minerals in the Cuprite mining district (Alunite HS295.3B, Buddingtonite GDS85 D-206, and Chalcodony CU91-6A), which are prominent in the Cuprite mining district. In this experiment, the regularization parameters used for SUnSAL and SUnSAL-DP were empirically set to the same  $\lambda = 0.002$ . The parameters of CLSUnSAL and CLSUnSAL-DP were set to the same  $\lambda = 0.02$ , while the parameters of SUnSAL-TV and SUnSAL-TV-DP were set to the same  $\lambda = 0.002$  and  $\lambda_{TV} = 0.002$ . The differences of fractional abundances estimated by SUnSAL and SUnSAL-DP were calculated (the same as for CLSUnSAL and CLSUnSAL-DP and SUnSAL-TV and SUnSAL-TV-DP).

As shown in Figs. 10–12, all three SUnSAL-DP, CLSUnSAL-DP, and SUnSAL-TV-DP are obtained very similar results, which are consistent with the results provided by the Tricorder 3.3 software product. This indicates that sparse unmixing algorithms can lead to good interpretation of the hyperspectral data. Furthermore, in order to analyze the performance of the proposed approach, Figs. 10–12 also present the difference maps between SUnSAL-DP and SUnSAL, CLSUnSAL-DP and CLSUnSAL, and SUnSAL-TV-DP and SUnSAL-TV. As can be seen from these figures, the difference mainly lives in the discontinuous regions, as expected. Finally, the *sparsity* values obtained by SUnSAL and SUnSAL-DP are 0.0678 and 0.0676, by CLSUnSAL and CLSUnSAL-DP are 0.0762 and 0.0757, and by SUnSAL-TV and SUnSAL-TV-DP are 0.0769 and 0.0751, respectively. These small differences lead to the conclusion that the proposed approach (by means of the inclusion of the edge information) uses a smaller number of elements to explain the data, thus enforcing higher sparsity. As a result, from a qualitative viewpoint, we can conclude that our newly introduced discontinuity-preserving strategy exhibits the potential to improve the results obtained by sparse unmixing in real analysis scenarios.

## VI. CONCLUSION

In this paper, a new discontinuity-preserving strategy has been developed to improve the accuracy of sparse unmixing by accounting for the spatial heterogeneity of endmember

abundances (particularly at the edges of image objects). The performance of our newly developed method, which aims at producing more realistic abundance estimations at the border of image objects, was evaluated using three simulated and one real hyperspectral data sets. Our experimental results consistently show that the newly developed discontinuity-preserving strategy for sparse unmixing can provide a better characterization of hyperspectral scenes by preserving the heterogeneity of abundance maps. Although the experimental results obtained in this paper are very encouraging, further experiments should be conducted to evaluate the method using additional real images. Our future work will focus on the development of other advanced edge methods to preserve the heterogeneity of abundance maps when conducting spectral unmixing.

## REFERENCES

- [1] D. Landgrebe, "Hyperspectral image data analysis," *IEEE Signal Process. Mag.*, vol. 19, no. 1, pp. 17–28, Jan. 2002.
- [2] G. Cheng and J. Han, "A survey on object detection in optical remote sensing images," *ISPRS J. Photogramm. Remote Sens.*, vol. 117, pp. 11–28, Jul. 2016.
- [3] G. Cheng, P. Zhou, and J. Han, "Learning rotation-invariant convolutional neural networks for object detection in VHR optical remote sensing images," *IEEE Trans. Geosci. Remote Sens.*, vol. 54, no. 12, pp. 7405–7415, Dec. 2016.
- [4] X. Yao, J. Han, G. Cheng, X. Qian, and L. Guo, "Semantic annotation of high-resolution Satellite images via weakly supervised learning," *IEEE Trans. Geosci. Remote Sens.*, vol. 54, no. 6, pp. 3660–3671, Jun. 2016.
- [5] P. Shippert, "Why use hyperspectral imagery?" *Photogramm. Eng. Remote Sens.*, vol. 70, no. 4, pp. 377–396, Apr. 2004.
- [6] J. M. Bioucas-Dias, A. Plaza, G. Camps-Valls, P. Scheunders, N. M. Nasrabadi, and J. Chanussot, "Hyperspectral remote sensing data analysis and future challenges," *IEEE Geosci. Remote Sens. Mag.*, vol. 1, no. 2, pp. 6–36, Jun. 2013.
- [7] J. M. Bioucas-Dias *et al.*, "Hyperspectral unmixing overview: Geometrical, statistical, and sparse regression-based approaches," *IEEE J. Sel. Topics Appl. Earth Observ. Remote Sens.*, vol. 5, no. 2, pp. 354–379, Apr. 2012.
- [8] N. Keshava and J. F. Mustard, "Spectral unmixing," *IEEE Signal Process. Mag.*, vol. 19, no. 1, pp. 44–57, Jan. 2002.
- [9] J. W. Boardman, F. A. Kruse, and R. O. Green, "Mapping target signatures via partial unmixing of AVIRIS data," in *Proc. JPL Airborne Earth Sci. Workshop*, 1995, pp. 23–26.
- [10] M. E. Winter, "N-FINDR: An algorithm for fast autonomous spectral end-member determination in hyperspectral data," *Proc. SPIE*, vol. 3753, pp. 266–275, Oct. 1999.
- [11] J. M. P. Nascimento and J. M. Bioucas-Dias, "Vertex component analysis: A fast algorithm to unmix hyperspectral data," *IEEE Trans. Geosci. Remote Sens.*, vol. 43, no. 4, pp. 898–910, Apr. 2005.
- [12] J. Li, A. Agathos, D. Zaharie, J. M. Bioucas-Dias, A. Plaza, and X. Li, "Minimum volume simplex analysis: A fast algorithm for linear hyperspectral unmixing," *IEEE Trans. Geosci. Remote Sens.*, vol. 53, no. 9, pp. 5067–5082, Sep. 2015.
- [13] M. Berman, H. Kiiveri, R. Lagerstrom, A. Ernst, R. Dunne, and J. F. Huntington, "ICE: A statistical approach to identifying endmembers in hyperspectral images," *IEEE Trans. Geosci. Remote Sens.*, vol. 42, no. 10, pp. 2085–2095, Oct. 2004.
- [14] J. M. P. Nascimento and J. M. Bioucas Dias, "Does independent component analysis play a role in unmixing hyperspectral data?" *IEEE Trans. Geosci. Remote Sens.*, vol. 43, no. 1, pp. 175–187, Jan. 2005.
- [15] N. Dobigeon, S. Moussaoui, M. Coulon, J.-Y. Tourneret, and A. O. Hero, "Joint Bayesian endmember extraction and linear unmixing for hyperspectral imagery," *IEEE Trans. Signal Process.*, vol. 57, no. 11, pp. 4355–4368, Nov. 2009.
- [16] F. Schmidt, A. Schmidt, E. Tréguier, M. Guiheneuf, S. Moussaoui, and N. Dobigeon, "Implementation strategies for hyperspectral unmixing using Bayesian source separation," *IEEE Trans. Geosci. Remote Sens.*, vol. 48, no. 11, pp. 4003–4013, Nov. 2010.

- [17] M.-D. Iordache, J. Bioucas-Dias, and A. Plaza, "Sparse unmixing of hyperspectral data," *IEEE Trans. Geosci. Remote Sens.*, vol. 49, no. 6, pp. 2014–2039, Jun. 2011.
- [18] F. Chen and Y. Zhang, "Sparse hyperspectral unmixing based on constrained  $l_p - l_2$  optimization," *IEEE Geosci. Remote Sens. Lett.*, vol. 10, no. 5, pp. 1142–1146, Sep. 2013.
- [19] Z. Shi, W. Tang, Z. Duren, and Z. Jiang, "Subspace matching pursuit for sparse unmixing of hyperspectral data," *IEEE Trans. Geosci. Remote Sens.*, vol. 52, no. 6, pp. 3256–3274, Jun. 2014.
- [20] K. E. Themelis, A. Rontogiannis, and K. D. Koutroumbas, "A novel hierarchical Bayesian approach for sparse semisupervised hyperspectral unmixing," *IEEE Trans. Signal Process.*, vol. 60, no. 2, pp. 585–599, Feb. 2012.
- [21] W. Tang, Z. Shi, Y. Wu, and C. Zhang, "Sparse unmixing of hyperspectral data using spectral *a priori* information," *IEEE Trans. Geosci. Remote Sens.*, vol. 53, no. 2, pp. 770–783, Feb. 2015.
- [22] F. Zhu, Y. Wang, S. Xiang, B. Fan, and C. Pan, "Structured sparse method for hyperspectral unmixing," *ISPRS J. Photogramm. Remote Sens.*, vol. 88, pp. 101–118, Feb. 2014.
- [23] C. Shi and L. Wang, "Incorporating spatial information in spectral unmixing: A review," *Remote Sens. Environ.*, vol. 149, pp. 70–87, Jun. 2014.
- [24] G. Martin and A. Plaza, "Spatial-spectral preprocessing prior to end-member identification and unmixing of remotely sensed hyperspectral data," *IEEE J. Sel. Topics Appl. Earth Observ. Remote Sens.*, vol. 5, no. 2, pp. 380–395, Apr. 2012.
- [25] G. Martin and A. Plaza, "Region-based spatial preprocessing for end-member extraction and spectral unmixing," *IEEE Geosci. Remote Sens. Lett.*, vol. 8, no. 4, pp. 745–749, Jul. 2011.
- [26] D. M. Rogge, B. Rivard, J. Zhang, A. Sanchez, J. Harris, and J. Feng, "Integration of spatial-spectral information for the improved extraction of endmembers," *Remote Sens. Environ.*, vol. 110, no. 3, pp. 287–303, 2007.
- [27] C. Deng and C. Wu, "A spatially adaptive spectral mixture analysis for mapping subpixel urban impervious surface distribution," *Remote Sens. Environ.*, vol. 133, pp. 62–70, Jun. 2013.
- [28] J. Franke, D. A. Roberts, K. Halligan, and G. Menz, "Hierarchical multiple endmember spectral mixture analysis (MESMA) of hyperspectral imagery for urban environments," *Remote Sens. Environ.*, vol. 113, no. 8, pp. 1712–1723, 2009.
- [29] M.-D. Iordache, J. Bioucas-Dias, and A. Plaza, "Total variation spatial regularization for sparse hyperspectral unmixing," *IEEE Trans. Geosci. Remote Sens.*, vol. 50, no. 11, pp. 4484–4502, Nov. 2012.
- [30] O. Eches, N. Dobigeon, and J.-Y. Tourneret, "Enhancing hyperspectral image unmixing with spatial correlations," *IEEE Trans. Geosci. Remote Sens.*, vol. 49, no. 11, pp. 4239–4247, Nov. 2011.
- [31] L. O. Jimenez, J. L. Rivera-Medina, E. Rodriguez-Diaz, E. Arzuaga-Cruz, and M. Ramirez-Velez, "Integration of spatial and spectral information by means of unsupervised extraction and classification for homogenous objects applied to multispectral and hyperspectral data," *IEEE Trans. Geosci. Remote Sens.*, vol. 43, no. 4, pp. 844–851, Apr. 2005.
- [32] S. Jia and Y. Qian, "Constrained nonnegative matrix factorization for hyperspectral unmixing," *IEEE Trans. Geosci. Remote Sens.*, vol. 47, no. 1, pp. 161–173, Jan. 2009.
- [33] E. J. Candès and T. Tao, "Decoding by linear programming," *IEEE Trans. Inf. Theory*, vol. 51, no. 12, pp. 4203–4215, Dec. 2005.
- [34] E. J. Candès and T. Tao, "Near-optimal signal recovery from random projections: Universal encoding strategies," *IEEE Trans. Inf. Theory*, vol. 52, no. 12, pp. 5406–5425, Dec. 2006.
- [35] J. Bioucas-Dias and M. A. T. Figueiredo, "Alternating direction algorithms for constrained sparse regression: Application to hyperspectral unmixing," in *Proc. 2nd Workshop Hyperspectral Image Signal Process., Evol. Remote Sens. (WHISPERS)*, Jun. 2010, pp. 1–4.
- [36] M.-D. Iordache, J. M. Bioucas-Dias, and A. Plaza, "Collaborative sparse regression for hyperspectral unmixing," *IEEE Trans. Geosci. Remote Sens.*, vol. 52, no. 1, pp. 341–354, Jan. 2014.
- [37] J. M. Prewitt, "Object enhancement and extraction," *Picture Process. Psychopictorics*, vol. 10, no. 1, pp. 15–19, 1970.
- [38] L.G. Roberts, "Machine perception of three-dimensional soups," Ph.D. dissertation, Massachusetts Inst. Technol., Cambridge, MA, USA, 1963.
- [39] L. J. van Vliet, I. T. Young, and G. L. Beckers, "A nonlinear Laplace operator as edge detector in noisy images," *Comput. Vis., Graph., Image Process.*, vol. 45, no. 2, pp. 167–195, 1989.
- [40] J. Canny, "A computational approach to edge detection," *IEEE Trans. Pattern Anal. Mach. Intell.*, vol. PAMI-8, no. 6, pp. 679–698, Nov. 1986.
- [41] J. Li, M. Khodadadzadeh, A. Plaza, X. Jia, and J. M. Bioucas-Dias, "A discontinuity preserving relaxation scheme for spectral-spatial hyperspectral image classification," *IEEE J. Sel. Topics Appl. Earth Observ. Remote Sens.*, vol. 9, no. 2, pp. 625–639, Feb. 2016.
- [42] M. Simoes, J. Bioucas-Dias, L. B. Almeida, and J. Chanussot, "A convex formulation for hyperspectral image superresolution via subspace-based regularization," *IEEE Trans. Geosci. Remote Sens.*, vol. 53, no. 6, pp. 3373–3388, Jun. 2015.
- [43] Z. Su, X. Luo, Z. Deng, Y. Liang, and Z. Ji, "Edge-preserving texture suppression filter based on joint filtering schemes," *IEEE Trans. Multimedia*, vol. 15, no. 3, pp. 535–548, Apr. 2013.
- [44] Y. Han, C. Xu, G. Baciú, and M. Li, "Lightness biased cartoon-and-texture decomposition for textile image segmentation," *Neurocomputing*, vol. 168, pp. 575–587, Nov. 2015.
- [45] N. Li, H. Huo, Y. M. Zhao, X. Chen, and T. Fang, "A spatial clustering method with edge weighting for image segmentation," *IEEE Geosci. Remote Sens. Lett.*, vol. 10, no. 5, pp. 1124–1128, Sep. 2013.
- [46] G. Liu, Y. Zhang, and A. Wang, "Incorporating adaptive local information into fuzzy clustering for image segmentation," *IEEE Trans. Image Process.*, vol. 24, no. 11, pp. 3990–4000, Nov. 2015.
- [47] S. He, Q. Yang, R. W. H. Lau, and M.-H. Yang, "Fast weighted histograms for bilateral filtering and nearest neighbor searching," *IEEE Trans. Circuits Syst. Video Technol.*, vol. 26, no. 5, pp. 891–902, May 2016.
- [48] S. Zhang, J. Li, K. Liu, C. Deng, L. Liu, and A. Plaza, "Hyperspectral unmixing based on local collaborative sparse regression," *IEEE Geosci. Remote Sens. Lett.*, vol. 13, no. 5, pp. 631–635, May 2016.
- [49] R. Feng, Y. Zhong, and L. Zhang, "An improved nonlocal sparse unmixing algorithm for hyperspectral imagery," *IEEE Geosci. Remote Sens. Lett.*, vol. 12, no. 4, pp. 915–919, Apr. 2015.
- [50] R. Feng, Y. Zhong, and L. Zhang, "Adaptive non-local Euclidean medians sparse unmixing for hyperspectral imagery," *ISPRS J. Photogramm. Remote Sens.*, vol. 97, pp. 9–24, Nov. 2014.
- [51] M.-D. Iordache, J. Bioucas-Dias, A. Plaza, and B. Somers, "MUSIC-CSR: Hyperspectral unmixing via multiple signal classification and collaborative sparse regression," *IEEE Trans. Geosci. Remote Sens.*, vol. 52, no. 7, pp. 4364–4382, Jul. 2014.
- [52] X. Fu, W.-K. Ma, J. M. Bioucas-Dias, and T.-H. Chan, "Semiblind hyperspectral unmixing in the presence of spectral library mismatches," *IEEE Trans. Geosci. Remote Sens.*, vol. 54, no. 9, pp. 5171–5184, Sep. 2016.
- [53] R. Clark *et al.*, "Imaging spectroscopy: Earth and planetary remote sensing with the USGS Tetracorder and expert systems," *J. Geophys. Res.*, vol. 108, no. E12, pp. 5131–5135, Dec. 2003.



**Shaoquan Zhang** (S'16) received the B.S. and M.E. degrees from the Nanchang Institute of Technology, Nanchang, China, in 2012 and 2015, respectively. He is currently pursuing the Ph.D. degree with the School of Geography and Planning, Sun Yat-sen University, Guangzhou, China.

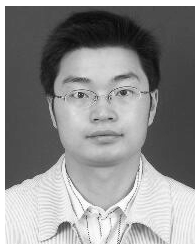
His research interests include hyperspectral unmixing, sparse representation, and machine learning.



**Jun Li** (M'12–SM'16) received the B.S. degree in geographic information systems from Hunan Normal University, Changsha, China, in 2004, the M.E. degree in remote sensing from Peking University, Beijing, China, in 2007, and the Ph.D. degree in electrical engineering from the Instituto de Telecomunicações, Instituto Superior Técnico (IST), Universidade Técnica de Lisboa, Lisbon, Portugal, in 2011.

From 2007 to 2011, she was a Marie Curie Research Fellow with the Departamento de Engenharia Electrotécnica e de Computadores, Instituto de Telecomunicações, IST, Universidade Técnica de Lisboa, in the framework of the European Doctorate for Signal Processing. She has also been actively involved in the Hyperspectral Imaging Network, a Marie Curie Research Training Network involving 15 partners in 12 countries and intended to foster research, training, and cooperation on hyperspectral imaging at the European level. Since 2011, she has been a Post-Doctoral Researcher with the Hyperspectral Computing Laboratory, Department of Technology of Computers and Communications, Escuela Politécnica, University of Extremadura, Cáceres, Spain. She is currently a Professor with Sun Yat-Sen University, Guangzhou, China. Her research interests include hyperspectral image classification and segmentation, spectral unmixing, signal processing, and remote sensing.

Dr. Li received several important awards and distinctions, including the IEEE Geoscience and Remote Sensing Society Early Career Award in 2017, due to her outstanding contributions to remotely sensed hyperspectral and synthetic aperture radar data processing. Since 2014, she has been an Associate Editor of the IEEE JOURNAL OF SELECTED TOPICS IN APPLIED EARTH OBSERVATIONS AND REMOTE SENSING. She has been a Guest Editor for several journals, including the PROCEEDINGS OF THE IEEE and the *ISPRS Journal of Photogrammetry and Remote Sensing*. She has also been an Active Reviewer for several journals, including the IEEE TRANSACTIONS ON GEOSCIENCE AND REMOTE SENSING, the IEEE GEOSCIENCE AND REMOTE SENSING LETTERS, and the IEEE TRANSACTIONS ON IMAGE PROCESSING.



**Zebin Wu** (M'13) received the B.Sc. and Ph.D. degrees in computer science and technology from the Nanjing University of Science and Technology, Nanjing, China, in 2003 and 2007, respectively.

From 2014 to 2015, he was a Visiting Scholar with the Hyperspectral Computing Laboratory, Department of Technology of Computers and Communications, Escuela Politécnica, University of Extremadura, Cáceres, Spain. He was a Visiting Scholar with the Department of Mathematics, University of California at Los Angeles, Los Angeles,

CA, USA, in 2016 and 2017. He is currently a Professor with the School of Computer Science and Engineering, Nanjing University of Science and Technology. His research interests include hyperspectral image processing, high-performance computing, and computer simulation.



**Antonio Plaza** (M'05–SM'07–F'15) received the M.Sc. and Ph.D. degrees in computer engineering from the Hyperspectral Computing Laboratory, Department of Technology of Computers and Communications, University of Extremadura, Cáceres, Spain, in 1999 and 2002, respectively.

He is currently the Head of the Hyperspectral Computing Laboratory, Department of Technology of Computers and Communications, University of Extremadura. He has authored or co-authored over 600 publications, including over 200 Journal Citation Reports journal papers (over 150 in IEEE journals), 24 book chapters, and over 300 peer-reviewed conference proceeding papers. His research interests include hyperspectral data processing and parallel computing of remote sensing data.

Dr. Plaza is a fellow of the IEEE for his contributions to hyperspectral data processing and parallel computing of Earth observation data. He was a member of the Editorial Board of the IEEE Geoscience and Remote Sensing Newsletter from 2011 to 2012 and the *IEEE Geoscience and Remote Sensing Magazine* in 2013. He was also a member of the Steering Committee of the IEEE JOURNAL OF SELECTED TOPICS IN APPLIED EARTH OBSERVATIONS AND REMOTE SENSING (JSTARS). He was a recipient of the recognition of Best Reviewers of the IEEE GEOSCIENCE AND REMOTE SENSING LETTERS in 2009, the IEEE TRANSACTIONS ON GEOSCIENCE AND REMOTE SENSING in 2010, the Most Highly Cited Paper in the *Journal of Parallel and Distributed Computing* from 2005 to 2010, the 2013 Best Paper Award of the JSTARS journal, the Best Column Award of the *IEEE Signal Processing Magazine* in 2015, and the Best Paper Awards at the IEEE International Conference on Space Technology and the IEEE Symposium on Signal Processing and Information Technology. He served as the Director of Education Activities and the President of the Spanish Chapter for the IEEE Geoscience and Remote Sensing Society from 2011 to 2012 and from 2012 to 2016, respectively. He was a guest editor for 10 special issues on hyperspectral remote sensing for different journals. He was a reviewer of over 500 papers for over 50 different journals. From 2007 to 2012, he served as an Associate Editor of the IEEE TRANSACTIONS ON GEOSCIENCE AND REMOTE SENSING. He is an Associate Editor of the IEEE ACCESS. He has served as the Editor-in-Chief of the IEEE TRANSACTIONS ON GEOSCIENCE AND REMOTE SENSING journal from 2013 to 2017. (Additional information: <http://www.umbc.edu/rssi/pl/people/aplaza>).